ADVANCED ENERGY MATERIALS
www.advenergymat.de

Reduction-Induced Oxygen Loss: the Hidden Surface Reconstruction Mechanism of Layered Oxide Cathodes in Lithium-Ion Batteries

Seungyun Jeon, Gukhyun Lim, Hoseok Lee, Hyunyoung Park, Min Kyung Cho, Chan Kim, YeEun Lee, Jaehoon Kim, Minhyung Kwon, Jung-Keun Yoo, Hyangsoo Jeong, Jinwoo Kim, Seung-Ho Yu, Minah Lee, Jongsoon Kim, and Jihyun Hong**

The surface reconstruction from the layered to rocksalt-type phase represents a primary deterioration pathway of layered-oxide cathodes in lithium-ion batteries, involving irreversible oxygen loss and transition metal migration. This degradation mechanism has primarily been attributed to the oxidative instability of highly delithiated cathodes at high voltages (>4.3 V vs Li/Li$^+$). However, the battery degradation also occurs under seemingly stable voltage ranges, the origin of which remains unclear. Herein, a hidden mechanism to induce surface reconstruction and oxygen loss is proposed, termed the "quasi-conversion reaction", which is revealed to occur during electrochemical reduction (discharge) processes just below 3.0 V (vs Li/Li$^+$). Combined experiments and first-principles calculations unveil that the oxygens at the surface can be extracted from the cathode lattice by forming lithium oxides and oxygen vacancies, at significantly higher potentials than conventional conversion reaction, due to the instability of surface oxygens coordinated with fewer cations than in the bulk. The chemical incompatibility between lithium oxides and commercial carbonate-based electrolytes results in electrolyte decomposition, forming an organic-rich blocking layer and gaseous byproducts, which further increases the cell impedance. This study emphasizes the necessity of a thorough understanding of surface instability upon reduction to develop long-lasting batteries.

1. Introduction

The energy density and cycle lives of lithium-ion batteries (LIBs) are determined by the number (or concentration) of lithium ions that the electrode material can reversibly store within its crystal structure, as well as the duration (or number of cycles) for which the crystal structure remains intact.[1,2] Commercial batteries restrict the concentration of lithium ions (or vacancies) in the cathode materials to an empirically derived stable range by controlling the charging voltage range, thereby preventing irreversible degradation of the crystal structure due to electrochemical reactions.[3,4] For representative layered oxide cathode materials, such as Li(Ni, Mn, Co)O_2 (NMC) and Li(Ni, Co, Al)O_2 (NCA), charge-discharge protocols have been developed to ensure the stable maintenance of the layered crystal structure and to prevent transition metal

S. Jeon, G. Lim, Y. Lee, J. Kim, M. Kwon, M. Lee, J. Hong
Department of Battery Engineering
Graduate Institute of Ferrous & Eco Materials Technology
Pohang University of Science and Technology (POSTECH)
Pohang 37667, Republic of Korea
E-mail: jhong@postech.ac.kr

S. Jeon, J. Kim
Center for Hydrogen Energy Materials
Korea Institute of Science and Technology (KIST)
Seoul 02792, Republic of Korea

S. Jeon, S.-H. Yu
Department of Chemical and Biological Engineering
Korea University
Seoul 02841, Republic of Korea

H. Lee, H. Park, J. Kim
Department of Energy Science
Sungkyunkwan University
Suwon 16419, Republic of Korea
E-mail: jongsoonkim@skku.edu

H. Lee, H. Park, J. Kim
SKKU Institute of Energy Science and Technology (SIEST)
Sungkyunkwan University
Suwon 16419, Republic of Korea

M. K. Cho
Advanced Analysis and Data Center
Korea Institute of Science and Technology (KIST)
Seoul 02792, Republic of Korea

C. Kim, H. Jeong
Center for Hydrogen and Fuel Cells
Korea Institute of Science and Technology
Seongbuk-gu, Seoul 02792, Republic of Korea

The ORCID identification number(s) for the author(s) of this article can be found under https://doi.org/10.1002/aenm.202404193

DOI: 10.1002/aenm.202404193

(TM) interlayer migration and cation mixing by leaving ≈30% of lithium ions within the cathode in the fully charged state.[5,6] The unwanted changes in the bulk crystal structure reduce the number of lithium storage sites and impede lithium migration, resulting in a permanent and kinetic decrease in capacity.[7–9]

A major strategy for maximizing the energy density of LIBs is increasing the charging cutoff voltages above 4.5 V (vs Li/Li^+).[10–13] When layered oxide cathodes, whose crystal structure (space group: R3$\bar{m}$) consists of TMO_2 slabs with layers of lithium in-between the slabs,[14] are charged to high voltages, the delithiation degree of $LiTMO_2$ increases, leading to accelerated material degradation.[13] It is revealed that the concentration of vacancies in the lithium layers exceeding a certain value or the oxidation of the active material beyond its manageable valence state leads to thermodynamic instability of the original layered structure. This instability causes TM cations from the TMO_2 slabs to migrate into the lithium layers, resulting in local coordination changes that stabilize the overall structure.[13,15,16] Additionally, a decrease in the concentration of lithium ions, which shields the repulsion between TMO_2 slabs, can lead to 2D sliding or rotation of the TMO_2 slabs, resulting in changes to the stacking sequence.[17,18] This material deformation can particularly intensify cation disordering in areas where strain is concentrated and is known to induce oxygen loss.[19] Moreover, the utilization of oxygen anion redox through high-voltage charging can lead to irreversible oxygen loss,[13,20] which forms the octahedral sites with oxygen vacancies. Due to the energetical instability of the defect in octahedral sites, TM cations tend to migrate to adjacent vacant octahedral sites in the lithium layer, causing the formation of a rocksalt phase at the particle surface, which hinders ion transfer.[21–23] Therefore, preventing oxygen loss is a critical mission that must be achieved to stabilize the cathode materials.

Fundamental insights to explaining the oxygen loss mechanism have been provided by existing theories, which mainly attribute oxygen loss in cathode materials to parasitic reactions between highly oxidized (delithiated) active materials and the electrolyte. These are suitable for explaining the degradation under high-voltage cycling. However, the layered-to-rocksalt surface reconstruction of actual NMC cathodes, which involves oxygen loss and stoichiometric changes, is often observed even within the stable electrochemical window of commercial electrolytes, i.e., <4.3 V (vs Li/Li^+).[24–28] The common observation of the rocksalt layer at the surface of cathode materials with various chemical compositions after long-term cycling leads us to hypothesize that there may be an additional, hidden mechanism for oxygen loss beyond the conventional oxygen release at high potential. The discovery of the hidden surface reconstruction mechanism, which is observed almost universally but often overlooked, could provide fundamental solutions for better preserving the crystal structure and electrochemical interfaces of cathodes and could play a crucial role in developing batteries with long cycle life.

Herein, for the first time, we unveil the reduction-induced surface oxygen loss mechanism in layered lithium TM oxides, which occurs at a "safe" potential range within the electrochemical window of commercial electrolytes. Through a systematic study of NMC cathodes cycled under conditions with various discharge cut-off voltages (DCOVs) and a constant charge cut-off potential (4.3 V vs Li/Li^+), we unambiguously demonstrate that the degradation of NMC primarily occurs at the particle surface near the end of discharge at a potential below 3.0 V. Density functional theory (DFT) calculations revealed that a new conversion-reaction-like pathway for $LiTMO_2$, such as NMC, forming TMO and Li_2O, which we notate as a quasi-conversion reaction. This reaction is possible at a potential between 2.0–3.0 V (vs Li/Li^+) on the surface of the materials with fewer coordinated oxygen anions. The potential for the quasi-conversion reaction depends on the local coordination elements of the surface oxygen anions and is higher for oxygens bonded with fewer Mn cations. Additionally, the quasi-conversion reaction leads to severe electrolyte decomposition at the particle surface, forming an organic-rich cathode-electrolyte interface (CEI) layer and gaseous byproducts. With the compounding effect of the ion-blocking rocksalt phase and high-resistance CEI layer, the charge-transfer resistance (R_{ct}) significantly increases under cycling conditions with lower DCOVs, resulting in poor cyclability. Our discovery emphasizes the critical importance of a systematic and precise setting of the DCOVs, which has been largely overlooked until now due to the minimal capacity in the 2.0–3.0 V range and the electrochemical stability of carbonate electrolytes. It also identifies an unprecedented surface degradation pathway in commercial electrode materials, providing an explanation for the inevitable battery degradation even under seemingly stable conditions.

2. Results and Discussion

2.1. Acceleration of Cathode Degradation Under the Conditions of Lower Discharge Cut-Off Voltages

Figure 1a shows the correlation between the cycle lives of $LiNi_{0.6}Mn_{0.2}Co_{0.2}O_2$ (hereafter, NMC622) cathodes and the discharge cut-off voltage in half cells. The NMC622 (Unicore corporation), consisting of secondary particles sized 9–14 μm (Figure S1, Supporting Information) and exhibiting high crystallinity with 3.6% Li/TM cation mixing (Figure S2 and Table S1, Supporting Information), was cycled as received. With the charge cut-off voltage fixed at 4.3 V, the various DCOVs were applied; 2.0 V (D2.0), 2.5 V (D2.5), 2.75 V (D2.75), 3.0 V (D3.0), and 3.25 V (D3.25). Interestingly, lowering the DCOV resulted in more severe capacity loss although the capacity accessible between 3.25–2.0 V is negligibly low, ≈6.2 mAh g^{-1}, corresponding to 0.022 Li per formula unit. The capacity retention of D2.0, D2.5, D2.75, D3.0, and D3.25 after 150 cycles was 75.4, 79.6, 83.3, 89.3, and 90.8%, respectively. With lower DCOVs, the cells experienced a

J.-K. Yoo
Energy Storage Research Center
Korea Institute of Science and Technology (KIST)
Seoul 02792, Republic of Korea
H. Jeong
Division of Energy and Environment Technology
KIST School
Korea University of Science and Technology
Seongbuk-gu, Seoul 02792, Republic of Korea
H. Jeong
KHU-KIST Department of Converging Science and Technology
Kyung Hee University
Dongdaemun-gu, Seoul 02447, Republic of Korea

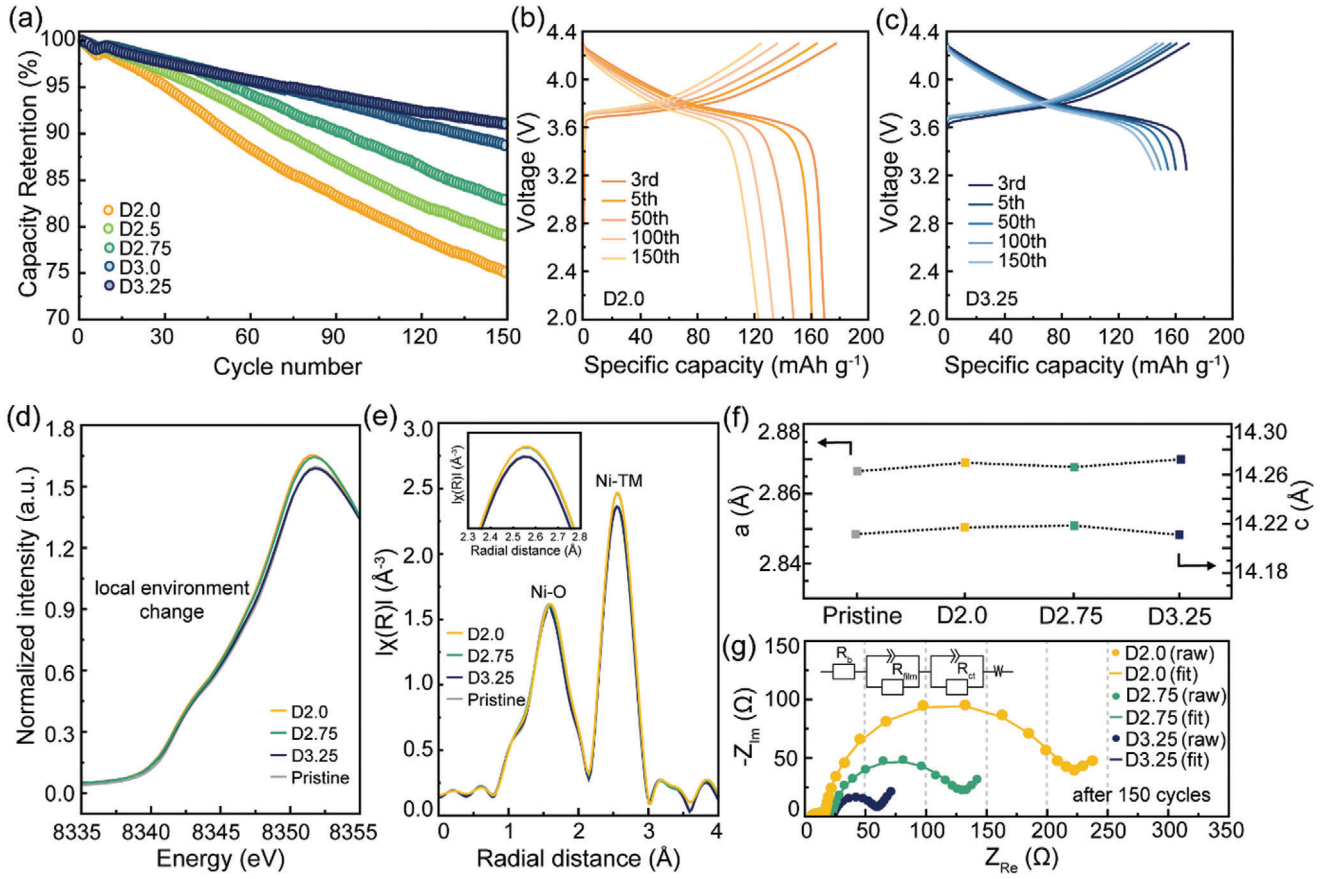

Figure 1. a) The capacity retention of NMC622 half cells tested in D2.0 (2.0–4.3 V), D2.5 (2.5–4.3 V), D2.75 (2.75–4.3 V), D3.0 (3.0–4.3 V), and D3.25 (3.25–4.3 V) at 0.5 C (1 C = 276.5 mA g^{-1}). The 3rd, 5th, 50th, 100th, and 150th voltage profiles of NMC622 half cells under the b) D2.0 and c) D3.25 conditions. d) Ni K-edge XANES spectra, e) Ni K-edge FT-EXAFS spectra, f) lattice parameters *a* and *c*, and g) EIS profiles of the pristine NMC622 and NMC622 after 150 cycles at 0.5 C within D2.0, D2.75, and D3.25. All cycled NMC622 electrodes were discharged to 3.25 V with CC-CV until reaching a current density of 0.01 C.

rapid and steady increase in overpotential during long-term cycling (Figures S3 and S4, Supporting Information). The degradation was particularly prominent when the DCOV was set below 3.0 V (Figure 1b–c; Figure S5, Supporting Information). Through cyclic voltammetry (CV) measurements, we observed that the overpotential after long-term cycling was significantly more pronounced under D2.0 conditions compared to D3.25 conditions (Figure S6, Supporting Information). This pronounced overpotential hinders the reversibility of the cells.[29–33] Note that the charge cut-off voltage of the cells was 4.3 V, which is a mild condition allowing high structural and electrochemical stability to NMC622 cathodes and carbonate-based commercial electrolytes, respectively.[24–28] As demonstrated in the linear sweep voltammetry (LSV) results, the commercial electrolyte remains stable not only up to the charging cutoff voltage of 4.3 V but also to the lowest DCOV of 2.0V (Figure S7, Supporting Information).

To understand the lithiation-induced degradation mechanism, the bulk chemistry and structure of the NMC622 cathodes after 150 cycles with various DCOVs were first investigated. We conducted X-ray absorption fine structure (XAFS, 10C Wide XAFS, PLS-II) spectroscopy to compare the local environment of TM. To minimize differences in the state of charge (SOC) for a fair comparison of irreversible degradation, all cells were discharged to 3.25 V with constant current-constant voltage (CC-CV) until the current density reached 0.01 C before the measurement. The X-ray absorption near-edge structure (XANES) spectra measured at the Ni K-edge show a minor change in Ni local environments after cycling at D2.0 and D2.75, whereas the spectra of D3.25 were identical to that of a pristine cathode (Figure 1d). Consistently, the extended X-ray absorption fine structure (EXAFS) spectra showed a slight increase in the relative intensity from the second nearest neighbors (Ni-TM) compared to that from the Ni—O bonds for D2.0 and D2.75 cathodes (Figure 1e). These results indicate that the low DCOV cycling may induce a lattice densification of the original layered structure, forming a structure with a higher TM to O ratio. The EXAFS spectra of Co and Mn K-edges showed similar relative intensity changes (Figure S8, Supporting Information), suggesting that structural evolution occurs non-selectively for all TM species in NMC622 when cycled with DCOVs below 3.0 V. Despite changes in the local structures, the X-ray diffraction (XRD) analysis barely shows differences in long-range ordering (Figure 1f; Figure S9, Supporting Information). The *a* and *c* lattice parameters measured by Rietveld refinements are similar across all conditions, ≈2.87 (±0.001535) Å and

14.22 (±0.004068) Å, respectively (see Table S2, Supporting Information for exact values). Overall, the bulk properties show only minor changes after cycling under D2.0 and D2.75 conditions. Despite the small differences, the electrochemical impedance spectroscopy (EIS) measurement demonstrates a significant contrast among the DCOVs (Figure 1g; Table S3, Supporting Information), implying the more severe overpotential and capacity fade shown under the lower DCOVs. The charge-transfer resistance (R_{ct}) after 150 cycles at D2.0, D2.75, and D3.25 conditions was 179.6, 92.95, and 29.69 Ω, respectively, suggesting more severe degradation at the surface than in the bulk of NMC622 after cycling.

2.2. Layered-to-Rocksalt Surface Reconstruction of NMC622 Facilitated at low Discharge Voltage

In **Figure 2**, we compare the atomic structure of the surface of NMC622 after 150 cycles with varied DCOVs using high-angle annular dark-field scanning transmission electron microscopy (HAADF-STEM) analyses. After cycling with a DCOV of 2.0 V (D2.0), a layered-to-rocksalt phase transformation occurred predominantly at the particle surface (Figure 2a). The fast-Fourier transform (FFT) patterns obtained near the surface (blue square) show bright diffraction spots from the rocksalt phase and dark ones from the original layered phase, indicated by yellow circles and green circles, respectively. See Figure S10 (Supporting Information) for the theoretically calculated FFT patterns of pure layered and rocksalt phases. To visualize the distribution of the original layered phase, we obtained the inverse FFT (IFFT) images by masking the spots corresponding to the layered phase that do not overlap with the spots from the rocksalt phase. The IFFT image displays a dark region at the particle surface, indicating a complete layered-to-rocksalt phase transition (Figure 2b). Figure 2c shows the intensity histogram along the white dotted lines in Figure 2a, comparing the TM occupancies in Li and TM layers. The histogram reveals negligible differences in the TM occupancies in Li and TM layers within 1 nm from the particle surface. Additionally, it indicates that TM migration occurred even at the 6 nm deep subsurface region of the D2.0 cathode. Similarly, the cathode cycled with a DCOV of 2.75 V (D2.75) underwent severe surface reconstruction (Figure 2d,e). However, the intensity histogram in Figure 2f shows higher TM occupancies in TM layers than in Li layers within 1 nm from the surface and a shallower propagation of cation disordering compared to D2.0.

In contrast to D2.0 and D2.75, the D3.25 cathode, which retained the highest capacity after long-term cycling (Figure 1a), maintained the layered structure without severe surface reconstruction. The HAADF-STEM image shows that cation mixing occurs in less than five atomic layers from the surface, and the FFT pattern shows bright spots from the layered phase even in the surface region (Figure 2g). The IFFT image confirms the well-preserved layered phase, except for a 1 nm thin dark region from the surface (Figure 2h). The negligible cation mixing in the D3.25 cathode is supported by the intensity histogram, which shows the TM occupancies in Li layers for the regions at 3 and 6 nm from the particle surface (Figure 2i). We note that the pristine NMC622 particles inherently possess a cation-disordered layer (<1 nm) at the surface (Figure S11, Supporting Information). The results indicate that the surface reconstruction has a significant correlation with the DCOVs, and avoiding deep discharge below 3.0 V effectively alleviates oxygen loss and cation disordering at the surface of layered oxides.

The soft X-ray absorption spectroscopy (sXAS) near-edge X-ray absorption fine structure (NEXAFS) spectra of the cycled NMC622, measured in total-electron yield (TEY) mode (probing depth ≤ 10 nm), reconcile the differences in surface reconstruction induced by DCOV control. The Ni L_3-edge NEXAFS spectra of the 4.3-V-charged NMC622 after cycling reveal a gradual increase in Ni^{2+} at the cathode surface from 43.7% to 66.1% as the cutoff voltage decreased from D3.25 to D2.0 (Figure 2j; Figure S12, Supporting Information). Consistently, the Mn L_3-edge NEXAFS spectra show that the reduction of the Mn cation became more pronounced at low DCOVs (Figure 2k), indicating the presence of a rocksalt phase with TMO stoichiometry. This tendency in the TM oxidation states is also reflected in the O K-edge spectra, which show reduced hole signals from $TM_{3d(eg)}$-O_{2p} hybrid orbitals (Figure 2l).[29,34,35]

In summary, the structural and chemical analyses using HAADF-STEM and sXAS consistently indicate the formation of a TM^{2+}-containing rocksalt phase, which requires significant O loss at the particle surface, when lowering the DCOVs. Thus, the accelerated capacity fade by lowered DCOVs is attributable to the lack of Li^+ conduction path in the rocksalt phase, impeding the charge transfer and increasing the overpotential. While the experimental observations consistently provide unambiguous results explaining the cause of electrochemical degradation, it is surprising that the control of DCOV between 2.0–3.25 V significantly alters the surface reconstruction mechanism, especially when considering the relatively small capacity (6.2 mAh g^{-1} = 0.022 Li per formula unit) accessible within the voltage range. The huge impact of a small fraction of electrochemical reaction on the overall cathode performance highlights the necessity of accurately understanding the mechanisms of parasitic reactions for realizing long-lasting batteries.

2.3. Reductive Surface Oxygen Release through Quasi-Conversion Reaction and Cascade Electrolyte Decomposition

Given the observations from structural and chemical probes, we hypothesize that surface reconstruction occurs through irreversible oxygen loss during electrochemical reduction processes below 3.0 V and above 2.0 V (vs Li/Li^+). While it is generally understood that charging layered oxide cathodes to high voltage (> 4.3 V vs Li/Li^+) triggers oxygen release from the lattice,[22,23,36–39] the reductive oxygen loss mechanism has been unprecedented. A conversion reaction, incorporating the complete reduction of TM oxides to form neutral metal (TM^0) and lithium oxide (Li_2O) mixed at a nanometer scale, is the only theory present to explain the reductive oxygen loss (**Figure 3a**).[40,41] However, conversion reactions of 3d-TM oxides occur at a low potential, typically below 1.0 V (vs Li/Li^+),[40–42] only applicable to anode materials.[43] To explain the oxygen loss induced by inserting lithium ions and electrons into the TM oxides, we propose a new mechanism called quasi-conversion reaction (Figure 3b). This mechanism involves a reduction

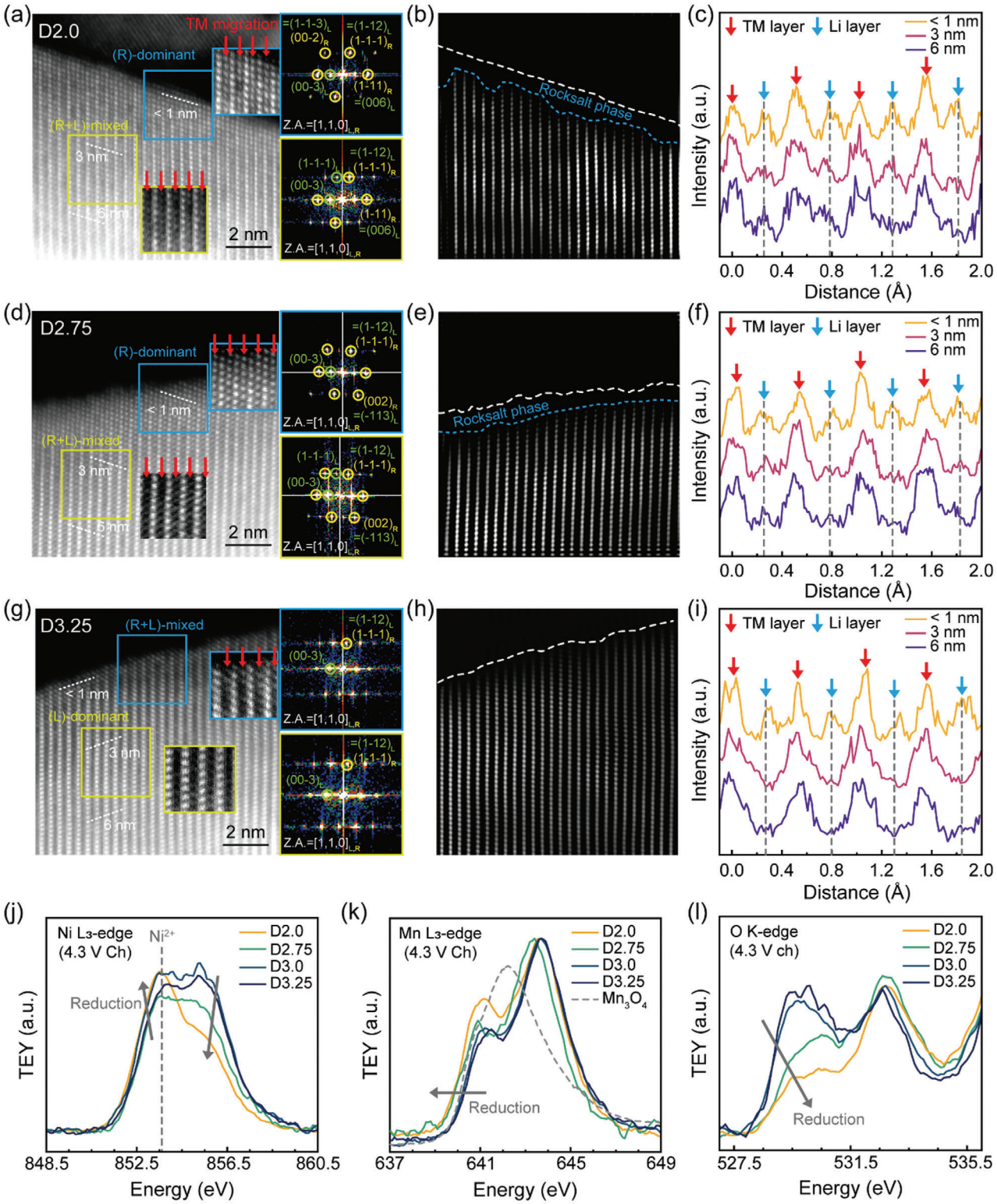

Figure 2. a) HAADF-STEM image of NMC622 electrode after 150 cycles at 0.5 C within D2.0 and corresponding FFT patterns of selected areas (each square area has 4 × 4 nm^2). b) IFFT image masked with spots relevant to (003) and (1-1-1) family planes of the layered phase. The empty space can be considered the region of the rocksalt phase. c) The intensity histogram of < 1, 3, and 6 nm lines indicated in the STEM image. d) HAADF-STEM image, e) IFFT image, and f) the intensity histogram of NMC622 after 150 cycles within D2.75. g) STEM image, h) IFFT image, and i) the intensity histogram of NMC622 after 150 cycles within D3.25. j) The Ni L_3-edge, k) Mn L_3-edge, and l) O K-edge sXAS spectra of the NMC622 electrodes cycled with D2.0, D2.75, D3.0, and D3.25.

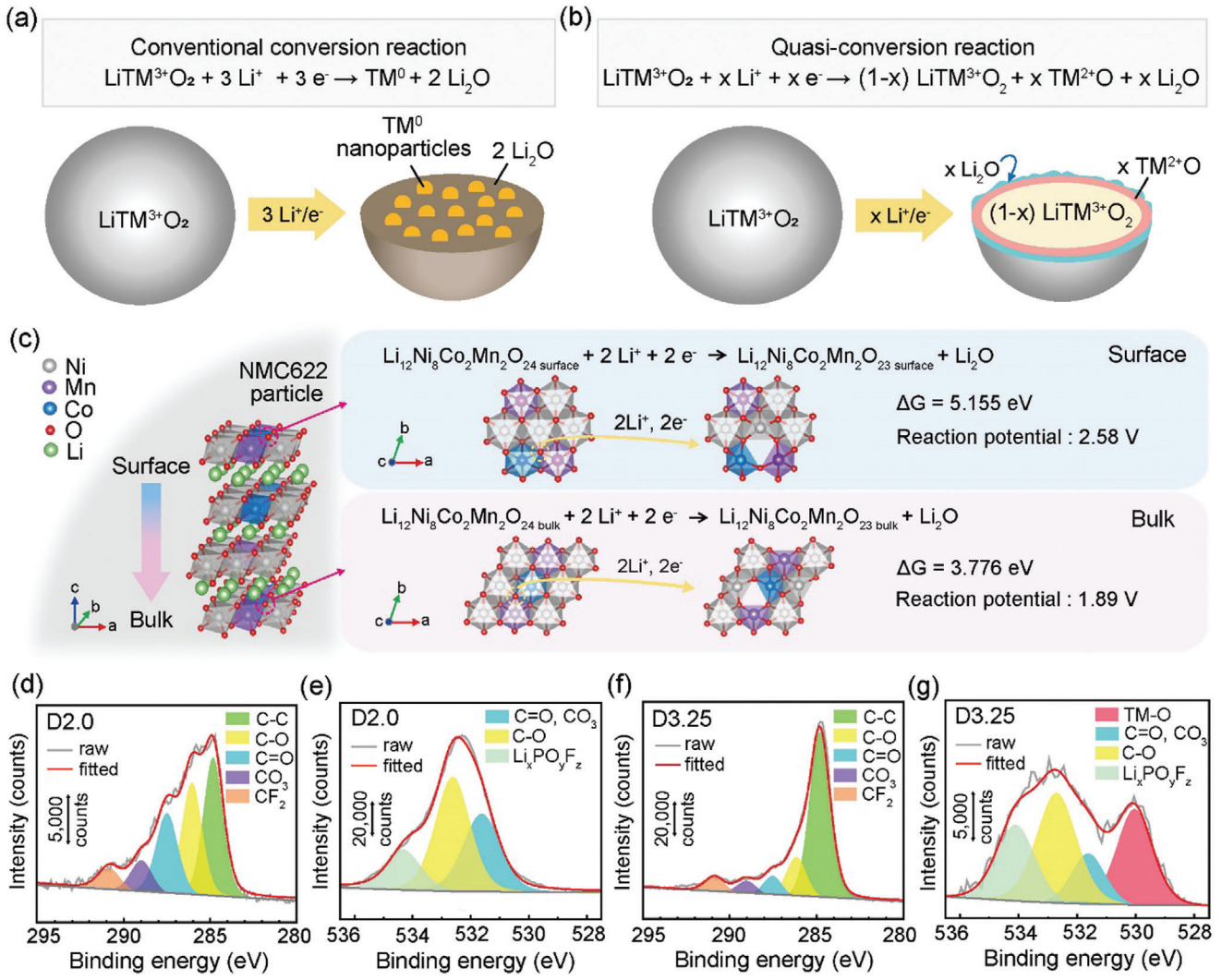

Figure 3. Equation and scheme of the a) conventional conversion reaction and b) quasi-conversion reaction. c) Illustration of oxygen release from the (003) surface and the bulk of NCM622 structure. The formation energy was converted to reaction potential according to the formula ΔG/number of electrons (see Figure S9, Supporting Information for the detailed value). XPS d) C 1s and e) O 1s spectra of the NMC622 electrode after 150 cycles at 0.5 C within D2.0. The carbonate solvent-related byproducts (C—O, C═O, and —CO_3) are observed at a depth of 6 nm. XPS f) C 1s and g) O 1s spectra of the NMC622 electrode after 150 cycles at 0.5 C within D3.25. Electrolyte decomposition is significantly mitigated in the D3.25 condition compared to the D2.0 condition.

process consisting of partial oxygen loss Equation (1) followed by a phase separation involving lattice densification Equation (2), which can be combined into an Equation (3):

$$LiTM^{3+}O_2{}^{surface} + xLi^+ + xe^- \rightarrow Li_{1-x}TM^{(3-x)+}O_{2-x}{}^{surface} + xLi_2O \quad (1)$$

$$Li_{1-x}TM^{(3-x)+}O_{2-x}{}^{surface} \rightarrow (1-x)\,LiTM^{3+}O_2{}^{sub-surface} + xTM^{2+}O^{surface} \quad (2)$$

$$LiTM^{3+}O_2{}^{surface} + xLi^+ + xe^- \rightarrow (1-x)\,LiTM^{3+}O_2{}^{sub-surface} + xTM^{2+}O^{surface} + xLi_2O \quad (3)$$

Using first-principles calculations, we investigated the potential for reduction-induced oxygen release at both the surface and the bulk of NMC622 to validate the proposed reaction mechanism. Surprisingly, the reduction potential for surface oxygen to form oxygen vacancy was, on average, 2.58 V for the oxygen coordinating with 3 TM cations at the surface (Figure 3c), which is significantly higher than the reduction potential for the conventional conversion reaction.[40–42] The high reaction potential indicates the high probability of the reaction occurring under general cycling conditions with a DCOV of 2.5 V [11,36] or below. In contrast, it is revealed that the potential of oxygen vacancy formation for the bulk oxygen was 1.89 V for the O coordinating with 3 TM and 3 Li cations (see Figure S13, Supporting Information for the formation energy values). Bader charge analyses reveal that the charge density of oxygen anions is lower at the surface compared

to the bulk, suggesting energetically more favorable oxygen decoordination at the cathode surface at a moderate voltage range due to the relatively weaker TM—O bonds (Figure S14, Supporting Information). We note that the resulting compounds consisting of lithium and oxygen possibly include lithium peroxide (Li_2O_2) and superoxide (LiO_2). However, both compounds are spontaneously reduced during discharge to form Li_2O at 2.86 and 2.88 V (vs Li/Li^+), respectively,[44,45] leading us to propose the most representative reaction path involving Li_2O formation for simplicity.

It has been revealed by Gallant and co-workers[46–48] that Li_2O is subject to continued chemical reaction with conventional carbonate electrolytes containing $LiPF_6$ salt, evolving to contain fluorine-rich ionic and organic phases at the electrode-electrolyte interface. To verify whether the quasi-conversion reaction, i.e., layered-to-rocksalt phase transition through oxygen release, provokes the formation of such solid-electrolyte-interphase (SEI)-like chemical components at the cathode surface, we performed X-ray photoelectron spectroscopy (XPS) analyses of NMC622 electrodes after 150 cycles under varied DCOVs. As expected, the XPS C 1s spectrum of the D2.0 (etched for 6 nm) exhibits sharp peaks at 286.1, 287.5, and 289.0 eV, indicating significant formation of byproducts with C—O, C═O, and —CO_3 bonds, respectively (Figure 3d; Table S4, Supporting Information).[49,50] Consistently, the O 1s spectrum of D2.0 shows intense peaks corresponding to electrolyte decomposition byproducts, while the TM-O peak at 529.9 eV is completely buried by the byproducts (Figure 3e). The XPS depth profiles of C 1s and O 1s (Figure S15, Supporting Information) indicate that the thickness of the byproduct layer exceeds at least 10 nm under the D2.0 condition, as no TM-O peak is observed after 10 nm of etching. In contrast, for the D3.25 condition, the C 1s and O 1s spectra show prominent peaks for C—C (conductive carbon) and TM—O (active material, NMC622) from the electrode surface after etching to ≈2–4 nm, suggesting that the byproduct layer is significantly thinner (Figure 3f,g; Figure S15c, Supporting Information).

This suggests that electrolyte decomposition is suppressed under the high-DCOV cycling protocol. A quantitative analysis reveals that the areal fractions of C—O, C═O, and —CO_3 peaks in the C 1s spectra of D2.0 (Table S4, Supporting Information), D2.75 (Figure S16 and Table S5, Supporting Information), and D3.25 (Table S6, Supporting Information) were 59.7, 47.6, and 32.5%, respectively. Given that the value for the NMC622 electrode immersed in electrolyte for 1 day was 29.8% (Figure S17 and Table S7, Supporting Information), the increase in the areal fraction was limited to 2.7% under the D3.25 condition. Therefore, we conclude that increasing the DCOV to 3.25 V effectively minimizes the quasi-conversion reaction and subsequent parasitic reactions, which is critical for maintaining the overpotential close to that of fresh batteries during long-term cycling.

2.4. Correlation between Oxygen Local Environment and Quasi-Conversion Reaction Potential

Since the surface reconstruction through quasi-conversion reaction necessitates oxygen loss, e.g., the decoordination of oxygen from TM species, it is reasonable to expect a correlation between the oxygen local environment and the potential of the cathodic oxygen loss. The dependency was systematically investigated by comparing the potential for four representative Ni-containing oxygen local environments in NMC622 using DFT calculations as shown in **Figure 4a**. When the oxygen is coordinated with 1Ni-1Co-1Mn, the reduction-induced oxygen loss occurs at 2.43 and 1.76 V (vs Li/Li^+) at the surface and bulk, respectively. Substituting Co with Ni in the coordination environment 2Ni-Mn shows minimal differences in the reaction potential, with values of 2.38 V for the surface and 1.74 V for the bulk. However, replacing Mn with Co (2Ni-Co) or Ni (3Ni) significantly increases the reaction potential for both the surface and bulk oxygen loss: 2.75 V (surface of 2Ni-Co), 2.07 V (bulk of 2Ni-Co), 2.78 V (surface of 3Ni), and 2.01 V (bulk of 3Ni). The results suggest that the oxygen becomes more prone to detachment from the lattice as Mn surrounding oxygen is replaced by Co or Ni, for both the surface and bulk.

Using DFT calculations on the $LiNi_{1/3}Mn_{1/3}Co_{1/3}O_2$ (NMC111) and $LiNi_{0.8}Mn_{0.1}Co_{0.1}O_2$ (NMC811) compositions (Figure S18, Supporting Information), we further reveal that for identical oxygen local environments, the potential for reductive oxygen loss is higher in Ni-richer NMCs than in Ni-poorer NMCs. For instance, in the 3Ni environment of NMC811, the surface and bulk reduction potentials of oxygen are 3.0 and 2.24 V, respectively, which are higher than the corresponding values of 2.78 and 2.01 V for NMC622, as shown in Figure 4a. All these results provide a theoretical explanation for the empirically observed poorer cyclability of Ni-richer NMCs, combined with the higher prevalence of oxygen environments surrounded by a greater proportion of nickel atoms in Ni-richer systems. These findings align with previous studies demonstrating the concentration gradient strategy to create Ni-poor and Mn-rich surfaces, which effectively mitigate degradation in Ni-rich cathode materials.[51–54]

The instability of the Mn-poor composition can be macroscopically examined by measuring the capacity retention of $LiNi_{0.8}Mn_{0.1}Co_{0.1}O_2$ (NMC811, Figure 4b) under the same cycling protocols for NMC622 (Figure 1a). After 140 cycles, NMC811 exhibits 82.2, 77.9, 73.3, 67.1, and 63.1% of the initial capacity under D3.25, D3.0, D2.75, D2.5, and D2.0 conditions, respectively. Analogous to NMC622, it is obvious that lowering the DCOV accelerates the capacity fade of NMC811 by inducing higher overpotential (Figure S19, Supporting Information), indicating the reduction-induced oxygen loss at the end of the discharge process. We note that the increase in degradation rate upon lowering DCOVs was higher in NMC811 than NMC622, which is likely attributable to more labile oxygens in NMC oxides with lower Mn contents. Combining the DFT calculations and experimental results, it becomes clear that adjusting the DCOVs is even more critical in Ni-rich compositions to prevent quasi-conversion reactions and improve cycle life characteristics.

2.5. Reinforced Degradation in Full Cells at Low DCOVs through Gaseous Byproduct Formation

To further verify the effect of DCOV control in practically feasible ultra-high-nickel cathode batteries, we fabricated and cycled three 1-Ah pouch full cells (6 × 9 cm^2, the cathode and anode are stacked with 3 and 4 sheets, respectively) consisting of $LiNi_{0.90}Mn_{0.04}Co_{0.06}O_2$ (NMC900406) and graphite (purchased

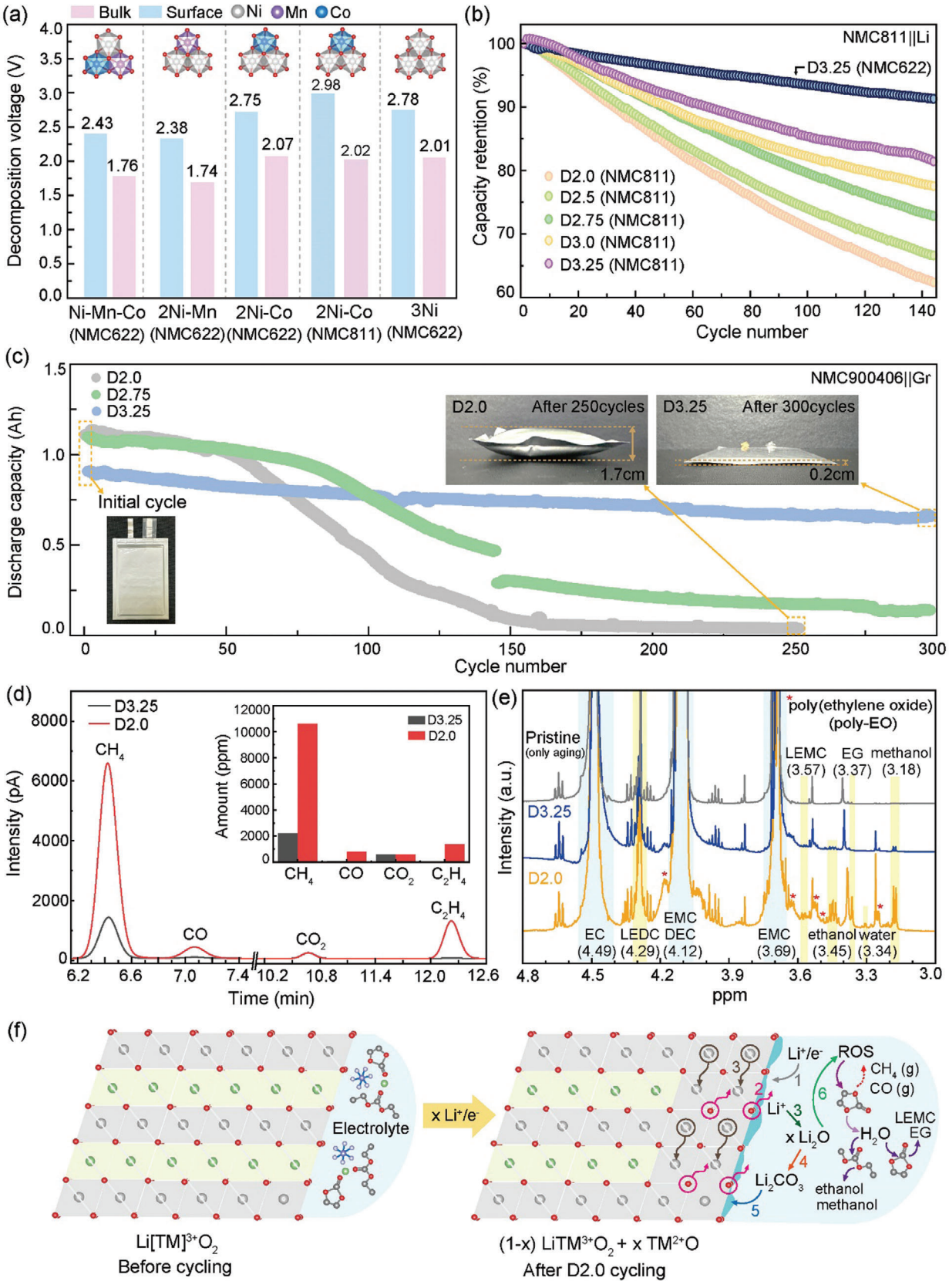

from Wellcos Corporation, Korea) under the conditions with varied DCOVs (Figure 4c). A negative 50 mV offset was applied to the full cells, so the D3.25, D2.75, and D2.0 conditions correspond to 4.25–3.15, 4.25–2.65, and 4.25–1.90 V cycling protocols, respectively. Under the D3.25 condition, the full cell exhibited excellent cycling stability with 73.4% capacity retention over 300 cycles at 0.5 C while the practical capacity of the cell was limited to 0.94 Ah, corresponding to 85% of the capacity accessible under the D2.0 condition. The cycle life of a practical pouch-type full cell, featuring a thick electrode (20 mg cm^{-2}) is comparable to those reported in previous studies.[55,56] When cycled under D2.75 and D2.0 conditions, the full cells retained 14.5% of capacity after 300 cycles and 3.8% after 250 cycles, respectively. The stark contrast in cycle lives and overpotential (Figure S20, Supporting Information) between the tested DCOVs corroborates the vital contribution of reduction-induced oxygen loss to the electrochemical stability of practical batteries. Despite the higher initial reversible capacity under D2.75 and D2.0 conditions, the accumulated capacity for 300 electrochemical cycles achieved under those conditions is equal to 47.8 and 69.9%, respectively, of that under the D3.25 condition (224.78 Ah, Figure S21 , Supporting Information). The results again emphasize the importance of the careful design of cycling protocols, particularly DCOV, whose impact on cathode degradation has been overlooked over the years.

It is worth noting that lowering DCOVs of the pouch-type full cell to 1.95 V caused severe swelling, involving the cell thickness change from 0.2 to 1.7 cm, indicating rigorous gas evolution as shown in the photographs of the cells after cycling (insets of Figure 4c). In contrast, the cell maintained its original thickness after 300 cycles under the D3.25 condition. Ex-situ gas chromatography (GC) analysis using a flame ionization detector (FID) (Figure 4d) and a thermal conductivity detector (TCD) (Figure S22, Supporting Information) reveals significant gas generation, including CH_4, CO, C_2H_4, H_2, and O_2, in the D2.0 pouch cell. The total amount of gases produced under the D2.0 condition is ≈29 times greater than that under the D3.25 condition. Specifically, the amounts of CH_4, CO, C_2H_4, H_2, and O_2 are 4.8, 10, 70, 7080, and 4.1 times higher, respectively, compared to the D3.25 pouch cell. These results suggest that the active quasi-conversion reaction under the D2.0 condition led to substantial oxygen evolution and promoted side reactions with the electrolyte. In addition, the pronounced generation of reducing gases such as CH_4, C_2H_2, and H_2 indicates that byproducts generated at the cathode migrated to the graphite anode, triggering active reduction reactions. Furthermore, ^{1}H NMR analysis (Figure 4e) reveals that, under the D2.0 condition, various byproducts—methanol, ethanol, lithium ethylene di-carbonate (LEDC), lithium ethylene mono-carbonate (LEMC), ethylene glycol (EG), poly(ethylene oxide) (poly-EO), and water—are dissolved in the electrolyte (Figure S23, Supporting Information), indicating severe electrolyte decomposition. By combining the byproducts identified through GC and NMR analyses, we inferred that reactive oxygen species (ROS, e.g., singlet $^1O_2$) actively reacted with the electrolyte solvent, initiating a cascade of reactions, including solvent hydrolysis (Figure S23, Supporting Information and Figure 4f).[57,58] The formation of these byproducts is coherent with the stimulated electrolyte decomposition and formation of C—O, C═O, and CO_3^{2-} containing residues at the cathode surface under the low DCOVs (Figure 3b–e). Additionally, we used an Inductively Coupled Plasma-Mass Spectrometry (ICP-MS) to measure the amount of transition metals (Ni, Co, Mn) dissolved from the cycled NMC900406 cathodes. The cathodes and separators recovered from the 1-Ah pouch cells cycled under D3.25 and D2.0 conditions were immersed in an equal volume solvent for 1 h. As shown in Figure S24 (Supporting Information), cycling under D2.0 conditions resulted in higher dissolution of all transition metals compared to cycling under D3.25 conditions.

We believe the intrinsic chemical incompatibility between the $LiPF_6$ contained carbonate electrolyte and Li_2O[46–48] produced via the quasi-conversion reaction contributes to the byproduct formation through electrolyte decomposition. The interfacial reaction between Li_2O and carbonate solvent in the presence of $LiPF_6$ leads the Li_2O interface to evolve into more stable SEI-like compounds, such as Li_2CO_3 and F-rich phases.[46–48] The decomposition of $LiPF_6$ produces PF_5 that again reacts with carbonate solvents to form species such as poly(ethylene oxide) and CO_2 gas. In addition, it is viable that the reaction between $LiPF_6$ and Li_2CO_3 results in the formation of LiF, POF_3, and CO_2.[46–48] Furthermore, it is reported by Li and co-workers[44] that the electrochemical oxidation of Li_2O to Li_2O_2 and LiO_2 occurs at ≈2.9 V in case Li_2O is contacted with metal oxides, and the solvated O_2^- (of LiO_2) can attack the methylene group of carbonate solvent via the so-called S_N2 mechanism.[59] The solvated O_2^- may provoke the ring-opening reaction of ethylene carbonate, forming a reactive peroxide radical in the electrolyte.[60] Another possible gas evolution scenario is the simultaneous electrochemical decomposition of carbonate electrolytes and lithium oxides (including Li_2O and Li_2O_2) during charging processes, which has been demonstrated by Amine et al., to occur at ≈4.0 V (vs Li/Li^+), incorporating the formation of mixed CO_2 and O_2 gaseous species and LiF, Li_2CO_3, and other byproducts.[61] Among the released O_2, reactive oxygen species such as singlet oxygen are known to readily decompose the electrolyte solvents, generating various gases such as CH_4, CO, and CO_2, together with soluble byproducts such as glycolic acid and oxalic acid.[20,58,62] Given that many previous reports have proven the severe instability of Li_2O in carbonate electrolytes, we conclude that it is practically impossible to directly observe Li_2O formed at the NMC cathode surface. Instead, the significant and continued formation of gaseous byproducts under the low DCOV conditions likely supports our proposed

Figure 4. a) Theoretical decomposition voltage for the (003) surface model and bulk model depending on the local environment surrounding the oxygen. b) The capacity retention of NMC811 half cells tested under D2.0 (2.0–4.3 V), D2.5 (2.5–4.3 V), D2.75 (2.75–4.3 V), D3.0 (3.0–4.3 V), and D3.25 (3.25–4.3 V) at 0.5 C (1C = 275.5 mA g^{-1}), in comparison with NMC622 cycled under D3.25. c) The cycling performance of 1-Ah NMC900406||graphite pouch cells tested in D2.0 (1.9–4.25 V), D2.75 (2.65–4.25 V), and D3.25 (3.15–4.25 V) at 0.5 C. Insets show the photogrphases of the pouch cell before and after cycling. d) GC-FID analysis for gases generated from 200th cycled 1-Ah NMC900406||graphite pouch cells. e) The ^{1}H NMR spectra of solutions containing electrolytes from 1-Ah NMC900406||graphite pouch cells (pristine cell and 200th cycled cells under D2.0 and D3.25, respectively). The asterisks (*) indicate peaks corresponding to poly(ethylene oxide) (poly-EO). f) A schematic illustration of the quasi-conversion reaction and cascade side reactions occurring in the cathode and electrolyte.

mechanism explaining the layered-to-rocksalt surface reconstruction stemming from the reduction-induced O loss at the surface of the cathode material (confirmed by STEM-EELS, Figure S25, Supporting Information) within the "conventional" electrochemical windows of commercial electrolytes. Furthermore, it is noteworthy that the accumulation of the quasi-conversion reaction, combined with a cascade of side reactions over prolonged cycling, leads to severe chemo-mechanical degradation of Ni-rich cathode materials with secondary morphology (Figures S26–S28, Supporting Information). We attribute the crack formation under low DCOV conditions to gaseous byproducts generated from electrolyte decomposition at the cathode-electrolyte interface, particularly in the spaces between primary particles where electrolyte penetration occurs. These findings highlight the importance of careful optimization of DCOV settings in lithium metal batteries—next-generation energy storage systems designed for higher energy density—where the depth-of-discharge is solely controlled by the cycling protocol due to the surplus of active lithium provided by the metallic anode.

3. Conclusion

In this work, we present a hidden surface oxygen loss mechanism that explains the origin of the near-universally observed layered-to-rocksalt surface reconstruction and the relatively worse long-term stability of Ni-richer layered oxides. We demonstrate that the surface of commercial layered oxide cathodes undergoes phase transformation and oxygen loss at the particle surface through a reduction (lithiation) process, named quasi-conversion reaction at the narrow-end of discharge processes. The potential of the reduction-coupled oxygen release was in the range of 2–3 V (vs Li/Li^+), which increases as the oxygen coordinates with fewer Mn cations in the first nearest neighbors, providing a reason for the worse cycle life of NMC811 than NMC622. The oxygen loss not only induces the structural transformation of the active material surface into the ionic-blocking rocksalt phase but also triggers the electrolyte decomposition at the cathode surface by forming highly reactive species. Both the rocksalt layer and the byproducts concurrently lead to the more sluggish reaction kinetics as the battery operates longer. By simply elevating the DCOVs, we realize a dramatic extension of cycle lives for 1-Ah NMC900406||graphite full cells, proposing an effective strategy to maintain the performances of the practical batteries. Our discovery also shows that the oxygen loss from NMC cathodes occurs during lithiation within the electrochemical stability window of commercial electrolytes. This possibility has been neglected due to well-established existing theories, emphasizing the need to revisit the DCOVs setting, which have often been arbitrarily applied in the 2.6–3.0 V (vs Li/Li^+) range.[54,63–67] Moreover, this study highlights the necessity of scientific understanding of the surface degradation mechanism of the electrode materials, which has remained relatively mysterious compared to the extensively established bulk degradation theories, for developing long-lasting batteries. We believe the complexity of the surface chemistry due to its intrinsic sensitivity to external conditions, such as current density, voltage, temperature, and even pressure has limited the fundamental understanding. Resolving the surface reconstruction mechanism will be an essential topic for future research, in addition to the existing practical approaches to improve the CEI stability through surface protection, doping, and electrolyte modification, for pushing the performance limits of the commercial LIB materials. Furthermore, by highlighting the significant impact of even a small fraction of electrochemical reactions on cell performance, this study demonstrates that the development of energy-dense batteries, including Ni-rich cathode batteries and lithium metal batteries (such as all-solid-state batteries), requires a thorough understanding of all electrochemical and chemical reactions occurring within the cell, no matter how minor.

Supporting Information

Supporting Information is available from the Wiley Online Library or from the author.

Acknowledgements

This work was supported by the Korea Planning & Evaluation Institute of Industrial Technology (KEIT) (RS-2024-00459497, Low-Expansion Mid-Nickel Material for Ultra-Long Cycle Life; RS-2022-00155717 Development of High-power Hybrid Lithium-ion Capacitors for Unmanned automatic Logistics Transport System) funded by the Ministry of Trade, Industry & Energy (MOTIE, Korea). This study was supported by the Korea Institute for Advancement of Technology (KIAT) grant funded by the Korea Government (MOTIE) (RS-2024-00419413, HRD Program for Industrial Innovation). This work was supported by the National Research Foundation of Korea (NRF) grant funded by the Korea government (MSIT) (RS-2024-00343810).

Conflict of Interest

The authors declare no conflict of interest.

Author Contributions

S.J. and G.L. contributed equally to this work. J.H., J.K. (Jongsoon Kim), S.J., and G.L. conceived the idea and designed the experiments. S.J. and G.L. prepared the samples did the electrochemical tests and performed materials characterization. H.L. and H.P. performed the DFT calculations. M.C. analyzed TEM and C.K. analyzed GC-FID. Y.L. and J.K. (Jaehoon Kim) prepared the samples and M.K. analyzed SEM. J.H., S.J., and G.L. wrote the manuscript. J.-K.Y, H.J., J.K. (Jinwoo Kim), S.-H.Y., and M.L. discussed the results and revised the manuscripts.

Data Availability Statement

The data that support the findings of this study are available from the corresponding author upon reasonable request.

Keywords

lithium-ion batteries, oxygen loss, quasi-conversion reaction, rocksalt formation, surface reconstruction

Received: September 13, 2024
Revised: December 31, 2024
Published online: January 16, 2025

[1] J. W. Choi, D. Aurbach, *Nat. Rev. Mater.* **2016**, *1*, 16013.
[2] M. G. Kim, J. Cho, *Adv. Funct. Mater.* **2009**, *19*, 1497.
[3] J.-M. Tarascon, M. Armand, *Nature* **2001**, *414*, 359.
[4] Y.-S. Kang, S. Y. Park, K. Ito, Y. Kubo, Y. Shin, D. Y. Kim, D.-H. Seo, S. Kim, J.-H. Park, S.-G. Doo, *J. Power Sources* **2021**, *490*, 229542.
[5] C. Xu, P. J. Reeves, Q. Jacquet, C. P. Grey, *Adv. Energy Mater.* **2021**, *11*, 2003404.
[6] L. Wang, G. Liu, R. Xu, X. Wang, L. Wang, Z. Yao, C. Zhan, J. Lu, *Adv. Energy Mater.* **2023**, *13*, 2203999.
[7] K. Kang, Y. S. Meng, J. Breger, C. P. Grey, G. Ceder, *Science* **2006**, *311*, 977.
[8] D. Eum, B. Kim, S. J. Kim, H. Park, J. Wu, S.-P. Cho, G. Yoon, M. H. Lee, S.-K. Jung, W. Yang, *Nat. Mater.* **2020**, *19*, 419.
[9] J. Huang, B. Ouyang, Y. Zhang, L. Yin, D.-H. Kwon, Z. Cai, Z. Lun, G. Zeng, M. Balasubramanian, G. Ceder, *Nat. Mater.* **2023**, *22*, 353.
[10] S.-T. Myung, F. Maglia, K.-J. Park, C. S. Yoon, P. Lamp, S.-J. Kim, Y.-K. Sun, *ACS Energy Lett.* **2017**, *2*, 196.
[11] W. Li, X. Liu, Q. Xie, Y. You, M. Chi, A. Manthiram, *Chem. Mater.* **2020**, *32*, 7796.
[12] S. Wolff-Goodrich, F. Lin, I. M. Markus, D. Nordlund, H. L. Xin, M. Asta, M. M. Doeff, *Phys. Chem. Chem. Phys.* **2015**, *17*, 21778.
[13] S. K. Jung, H. Gwon, J. Hong, K. Y. Park, D. H. Seo, H. Kim, J. Hyun, W. Yang, K. Kang, *Adv. Energy Mater.* **2014**, *4*, 1300787.
[14] X. Gao, J. Guo, S. Li, H. Zhang, Y. Zhang, C. Guan, M. Wang, Y. Lai, Z. Zhang, *Small* **2024**, *20*, 2401132.
[15] J. Lee, A. Urban, X. Li, D. Su, G. Hautier, G. Ceder, *Science* **2014**, *343*, 519.
[16] J. Hong, W. E. Gent, P. Xiao, K. Lim, D.-H. Seo, J. Wu, P. M. Csernica, C. J. Takacs, D. Nordlund, C.-J. Sun, *Nat. Mater.* **2019**, *18*, 256.
[17] J.-H. Song, S. Yu, B. Kim, D. Eum, J. Cho, H.-Y. Jang, S.-O. Park, J. Yoo, Y. Ko, K. Lee, *Nat. Commun.* **2023**, *14*, 4149.
[18] R. A. House, U. Maitra, M. A. Pérez-Osorio, J. G. Lozano, L. Jin, J. W. Somerville, L. C. Duda, A. Nag, A. Walters, K.-J. Zhou, *Nature* **2020**, *577*, 502.
[19] C. Wang, X. Wang, R. Zhang, T. Lei, K. Kisslinger, H. L. Xin, *Nat. Mater.* **2023**, *22*, 235.
[20] R. Jung, M. Metzger, F. Maglia, C. Stinner, H. A. Gasteiger, *J. Electrochem. Soc.* **2017**, *164*, A1361.
[21] A. Urban, J. Lee, G. Ceder, *Adv. Energy Mater.* **2014**, *4*, 1400478.
[22] H. Wan, Z. Liu, G. Liu, S. Yi, P. Yan, H. Deng, W. Hu, F. Gao, *Nano Lett.* **2021**, *21*, 6875.
[23] S. K. Jung, H. Kim, S. H. Song, S. Lee, J. Kim, K. Kang, *Adv. Funct. Mater.* **2022**, *32*, 2108790.
[24] F. Lin, I. M. Markus, D. Nordlund, T.-C. Weng, M. D. Asta, H. L. Xin, M. M. Doeff, *Nat. Commun.* **2014**, *5*, 3529.
[25] J. Y. Park, M. Jo, S. Hong, S. Park, J. H. Park, Y. I. Kim, S. O. Kim, K. Y. Chung, D. Byun, S. M. Kim, *Adv. Energy Mater.* **2022**, *12*, 2201151.
[26] P. Hu, J. Zhao, T. Wang, C. Shang, J. Zhang, B. Qin, Z. Liu, J. Xiong, G. Cui, *Electrochem. Commun.* **2015**, *61*, 32.
[27] A. Manthiram, J. C. Knight, S. T. Myung, S. M. Oh, Y. K. Sun, *Adv. Energy Mater.* **2016**, *6*, 1501010.
[28] H.-H. Ryu, B. Namkoong, J.-H. Kim, I. Belharouak, C. S. Yoon, Y.-K. Sun, *ACS Energy Lett.* **2021**, *6*, 2726.
[29] G. Lim, D. Shin, K. H. Chae, M. K. Cho, C. Kim, S. S. Sohn, M. Lee, J. Hong, *Adv. Energy Mater.* **2022**, *12*, 2202049.
[30] G. Lim, M. K. Cho, J. Choi, K.-J. Zhou, D. Shin, S. Jeon, M. Kwon, A.-R. Jeon, J. Choi, S. S. Sohn, *Energy Environ. Sci.* **2024**, *29*, 2401132.
[31] S. K. Singh, D. Dutta, R. K. Singh, *Electrochim. Acta* **2020**, *343*, 136122.
[32] R. Mishra, R. K. Tiwari, A. Patel, A. Tiwari, R. K. Singh, *J. Energy Storage* **2024**, *77*, 110058.
[33] H. Gupta, R. K. Singh, *Chem. Electro. Chem.* **2020**, *7*, 3597.
[34] M. Oishi, C. Yogi, I. Watanabe, T. Ohta, Y. Orikasa, Y. Uchimoto, Z. Ogumi, *J. Power Sources* **2015**, *276*, 89.
[35] Z. Yang, L. Mu, D. Hou, M. M. Rahman, Z. Xu, J. Liu, D. Nordlund, C. J. Sun, X. Xiao, F. Lin, *Adv. Energy Mater.* **2021**, *11*, 2002719.
[36] S. H. Song, M. Cho, I. Park, J. G. Yoo, K. T. Ko, J. Hong, J. Kim, S. K. Jung, M. Avdeev, S. Ji, *Adv. Energy Mater.* **2020**, *10*, 2000521.
[37] K. Ku, J. Hong, H. Kim, H. Park, W. M. Seong, S. K. Jung, G. Yoon, K. Y. Park, H. Kim, K. Kang, *Adv. Energy Mater.* **2018**, *8*, 1800606.
[38] W. E. Gent, K. Lim, Y. Liang, Q. Li, T. Barnes, S.-J. Ahn, K. H. Stone, M. McIntire, J. Hong, J. H. Song, *Nat. Commun.* **2017**, *8*, 2091.
[39] L. Fang, D. Han, S. Kang, U.-S. Heo, K.-W. Nam, Y.-M. Kang, *Energy Environ. Sci.* **2023**, *16*, 3053.
[40] J. Shu, M. Shui, F. Huang, Y. Ren, Q. Wang, D. Xu, L. Hou, *J. Phys. Chem. C* **2010**, *114*, 3323.
[41] J. N. Weker, A. M. Wise, K. Lim, B. Shyam, M. F. Toney, *Electrochim. Acta* **2017**, *247*, 977.
[42] L. Yu, Y. Tian, X. Xiao, C. Hou, Y. Xing, Y. Si, H. Lu, Y. Zhao, *J. Electrochem. Soc.* **2021**, *168*, 050516.
[43] S.-i. Okuoka, Y. Ogasawara, Y. Suga, M. Hibino, T. Kudo, H. Ono, K. Yonehara, Y. Sumida, Y. Yamada, A. Yamada, *Sci. Rep.* **2014**, *4*, 5684.
[44] Z. Zhu, A. Kushima, Z. Yin, L. Qi, K. Amine, J. Lu, J. Li, *Nat. Energy* **2016**, *1*, 16111.
[45] Y. Qiao, H. Deng, P. He, H. Zhou, *Joule* **2020**, *4*, 1445.
[46] R. Guo, D. Wang, L. Zuin, B. M. Gallant, *ACS Energy Lett.* **2021**, *6*, 877.
[47] L. Droguet, G. M. Hobold, M. F. Lagadec, R. Guo, C. Lethien, M. Hallot, O. Fontaine, J.-M. Tarascon, B. M. Gallant, A. Grimaud, *ACS Energy Lett.* **2021**, *6*, 2575.
[48] K. Steinberg, B. M. Gallant, *J. Electrochem. Soc.* **2024**, *171*, 080530.
[49] W. Zhao, J. Zheng, L. Zou, H. Jia, B. Liu, H. Wang, M. H. Engelhard, C. Wang, W. Xu, Y. Yang, *Adv. Energy Mater.* **2018**, *8*, 1800297.
[50] N. D. Phillip, C. Daniel, G. M. Veith, *J. Electrochem. Soc.* **2020**, *167*, 040521.
[51] Z. Huang, J. Yan, Z. Liu, W. Wang, Y. Tang, Z. Zhang, T. Yang, X. Wang, X. Li, Q. Kong, *Adv. Funct. Mater.* **2024**, *34*, 2400956.
[52] U. H. Kim, H. H. Ryu, J. H. Kim, R. Mücke, P. Kaghazchi, C. S. Yoon, Y. K. Sun, *Adv. Energy Mater.* **2019**, *9*, 1803902.
[53] N. Y. Park, G. Cho, S. B. Kim, Y. K. Sun, *Adv. Energy Mater.* **2023**, *13*, 2204291.
[54] H.-H. Ryu, H.-W. Lim, S. G. Lee, Y.-K. Sun, *Nat. Energy* **2024**, *9*, 47.
[55] F. Reissig, J. Ramirez-Rico, T. J. Placke, M. Winter, R. Schmuch, A. Gomez-Martin, *Batteries* **2023**, *9*, 245.
[56] A. Gomez-Martin, F. Reissig, L. Frankenstein, M. Heidbüchel, M. Winter, T. Placke, R. Schmuch, *Adv. Energy Mater.* **2022**, *12*, 2103045.
[57] B. L. Rinkel, J. P. Vivek, N. Garcia-Araez, C. P. Grey, *Energy Environ. Sci.* **2022**, *15*, 3416.
[58] B. L. Rinkel, D. S. Hall, I. Temprano, C. P. Grey, *J. Am. Chem. Soc.* **2020**, *142*, 15058.
[59] V. S. Bryantsev, M. Blanco, *J. Phys. Chem. Lett.* **2011**, *2*, 379.
[60] S. A. Freunberger, Y. Chen, Z. Peng, J. M. Griffin, L. J. Hardwick, F. Bardé, P. Novák, P. G. Bruce, *J. Am. Chem. Soc.* **2011**, *133*, 8040.
[61] T. Zhang, R. Amine, X. Bi, Y. Qin, M. Li, S. Al-Hallaj, F. Huo, J. Lu, K. Amine, *J. Mater. Chem. A* **2019**, *7*, 15615.
[62] W. M. Dose, I. Temprano, J. P. Allen, E. Björklund, C. A. O'Keefe, W. Li, B. L. Mehdi, R. S. Weatherup, M. F. De Volder, C. P. Grey, *ACS Appl. Mater. Interfaces* **2022**, *14*, 13206.
[63] C. Niu, H. Lee, S. Chen, Q. Li, J. Du, W. Xu, J.-G. Zhang, M. S. Whittingham, J. Xiao, J. Liu, *Nat. Energy* **2019**, *4*, 551.
[64] C. Niu, H. Pan, W. Xu, J. Xiao, J.-G. Zhang, L. Luo, C. Wang, D. Mei, J. Meng, X. Wang, *Nat. Nanotechnol.* **2019**, *14*, 594.
[65] T. Yang, K. Zhang, Y. Zuo, J. Song, Y. Yang, C. Gao, T. Chen, H. Wang, W. Xiao, Z. Jiang, *Nat. Sustain.* **2024**, *7*, 1204.
[66] Z. Cui, P. Zuo, Z. Guo, C. Wang, A. Manthiram, *Adv. Mater.* **2024**, *36*, 2402420.
[67] H. Park, H. Park, K. Song, S. H. Song, S. Kang, K.-H. Ko, D. Eum, Y. Jeon, J. Kim, W. M. Seong, *Nat. Chem.* **2022**, *14*, 614.